Fast Synthesis of Breast Monostatic Microwave Response for Massive Dataset Generation

Raquel A. Martins, João M. Felício, *Member, IEEE*, Jorge R. Costa, *Senior Member, IEEE*, and Carlos A. Fernandes, *Life Senior Member, IEEE*

***Abstract*—Microwave (MW) technology has been researched for the past decades as a promising technique for breast cancer detection. However, its value for the medical community compared to existing techniques is still undetermined. One of the reasons is the lack of large enough representative datasets of MW signals for evaluation and improvement of the developed signal processing algorithms. To overcome this, we present a fast hybrid method combining geometrical optics, physical optics and full-wave analysis that can model the direct problem, allowing us to create digital twins of experimental microwave monostatic setups, for fast generation of large representative datasets. For validation purposes, a digital twin of our in-house experimental dry microwave setup was implemented – *MWSensing* – and made openly available to the interested community. We have tested the model against experimental results in the 2-5 GHz range for cylindrical, elliptical and anthropomorphic, homogeneous and heterogeneous breasts phantoms, with a tumor placed inside, in different positions. We show that the MW signals obtained from *MWSensing* and from the experimental setup are of the same nature and provide similar imaging results. With this framework, it becomes possible to build a large dataset of MW signals, quickly and efficiently, enabling users to evaluate firsthand their algorithms before moving on to more advanced test stages.**

***Index Terms*—Breast cancer diagnosis, microwave imaging, ray tracing, physical optics, digital twin.**

I. Introduction

MICROWAVE imaging (MW) has been explored as a complementary modality to conventional breast screening techniques because of more favorable contrast between tumor and background tissues compared to X-rays, further to being non-ionizing, non-invasive, potentially automatable and low-cost [1], [2], [3], [4]. However, the response from the high permittivity contrast between skin and air dominates the received signals [4] and needs to be properly addressed to separate the weak tumor response. Studies have also shown that reasonable penetration of breast tissues can only be achieved for frequencies in the 1 to 8 GHz interval, which limits the image resolution. As shown by the authors in [5], this also complicates the distinction between benign and malignant tumors. These are some aspects that may limit tumor detection using microwaves.

The breast imaging community has been analyzing and developing algorithms for the past decades, to tackle these difficulties. Simulation-based studies use full-wave methods, involving heavy computational effort. For this reason, they are usually performed on simplified breast models [6], [7], [8], [9] or a small number of complete 2D breast numerical models [10], [11], which may not represent correctly the variability of real data.

Some research groups are working with experimental data obtained in a laboratory environment [4], [11], [12], [13]. But their results, obtained on a limited number of models, may not be applicable to all breast conditions. To help the breast community progress, authors in [14] have created an open-access database with 66 anthropomorphic breasts out of a total of 1257 breast scans. This number can still be considered limited in view of the complexity of the breast structure. When testing ML algorithms, some authors use data augmentation techniques [11], [13] to increase signal variability. However, this is a challenging process, since the modified signals may not be representative or add useful information to the initial group of phantoms.

Clinical trials have been emerging, showing promising results for the development of this technology [15], [16], [17]. However, current clinical systems have different configurations (e.g., different frequency ranges, number of antennas, and use different signal processing techniques), making it difficult to compare results. Moreover, not many of these datasets were made publicly available. This has been delaying conclusions about e.g., sensitivity and specificity of MW-based tumor detection, to understand its medical value.

For this reason, it would be of great interest to have available a computationally fast method capable of generating massive representative MW scattering data, with free choice of phantom configurations and setup parameters. This is the motivation of the present paper. For that, we present a simplified formalism for solving the direct problem: the calculation of the breast scattering response from its known geometry and materials. The proposed method combines geometrical optics and physical optics modelling with full-wave tumor scattering characterization.

Received 8 August 2025; revised 18 December 2025; accepted 11 January 2026. Date of publication 16 February 2026; date of current version 21 May 2026. This work was suppported by Fundação para a Ciência e Tecnologia (FCT/MCTES) through National Funds under Scholarship SFRH/BD/144961/2019 and in part by FEDER under Project UIDB/50008/2020 and Project 2022.04764.PTDC through IRMIS. *(Corresponding author: Raquel A. Martins.)*

Raquel A. Martins, João M. Felício, and Carlos A. Fernandes are with the Instituto de Telecomunicações, Instituto Superior Técnico (IT-IST), Universidade de Lisboa, 1049-001 Lisbon, Portugal (e-mail: raquel.martins@lx.it.pt; joao.felicio@lx.it.pt; carlos.fernandes@lx.it.pt).

Jorge R. Costa is with the Telecomunicações, Instituto Superior Técnico (IT-IST), Universidade de Lisboa, 1049-001 Lisbon, Portugal, and also with the Instituto Universitário de Lisboa (ISCTE-IUL), 1649-026 Lisbon, Portugal (e-mail: jorge.costa@iscte-iul.pt).

Digital Object Identifier 10.1109/JERM.2026.3654946

© 2026 The Authors. This work is licensed under a Creative Commons Attribution 4.0 License. For more information, see https://creativecommons.org/licenses/by/4.0/

The latter feature may be very relevant for modeling the tumor malignancy, which would otherwise be impossible to account for, using an empirical representation.

The method is demonstrated by comparing the experimental results obtained in an air operated MW breast imaging setup developed in our lab, with the corresponding digital twin based on the proposed model. The digital twin code, written in MatLab – *MWSensing* – is available open-access [18]. It includes a user-friendly graphical user interface, and allows the user to control different parameters, input and output data, and provides results for each analyzed breast within a few seconds. To the best of our knowledge, this is the first open-access digital twin tool that allows fast generation of representative MW signals, favoring the evaluation of signal/imaging algorithms and others (e.g., ML algorithms).

In this study, the digital twin was implemented to replicate our laboratory setup, which employs a single antenna rotating around the breast phantom at fixed positions and operating frequencies. These parameters were held constant to enable direct validation against experimental data. The modeling was explicitly based on the experimental phantoms available to us. However, the modeling framework is general and can be adapted to other scenarios by adjusting the user-defined input parameters and the model's four calibration coefficients according to the proposed procedure. This ensures that the simulated geometries are not arbitrary but grounded in realistic phantom designs. While clinical translation will require strategies to manage the full variability of breast anatomy, the use of experimentally grounded phantoms provides a practical and representative basis for early stage systematic studies.

There is a freely available microwave breast simulator [19], but it considers only homogeneous circular breasts with circular tumors. There are also two open-source toolboxes available (MERIT [20] and *MWSegEval* [21]) but focused on post-processing methods i.e., signal processing and imaging analysis.

II. Method Formulation

We consider a monostatic approach, where a single antenna $a$illuminates the breast successively from N_a equally spaced positions over a circumference, and receives the scattered energy due to the contrast of dielectric properties between tissues, manifested in the complex-valued input reflection $s_{11}(f)$ at the antenna port.

Our method resembles the hybrid geometrical optics–physical approach (GO-PO), where ray tracing is used to illuminate the surfaces, and the scattering response is obtained by integration of the fields on those surfaces. The tumor radar cross-section (RCS) is treated by full-wave. Ray tracing is generally applicable for the far field, however ray propagation approximation for the breast near-field has shown satisfactory results with inverse algorithms and it is widely accepted in the literature for this.

The $s_{11}(f)$ of an antenna in the presence of the breast is a sum of the antenna internal reflections $\Gamma_a(f)$ and all the external reflections occurring along the ray trajectory: at the breast external boundary $b_s(f)$, at the fibroglandular tissue boundary $b_g(f)$, at the tumor $b_t(f)$ and at the back wall of the breast $b_w(f)$ (see Fig. 1). To account for system uncertainty, we explicitly include an additive noise term η, which represents Gaussian noise contributions from the measurement setup (e.g., vector network analyzer noise floor, position perturbations, etc). In our formulation, this noise parameter is set to around –90 dB, consistent with the used VNA intermediate frequency bandwidth configuration and signal averaging index.

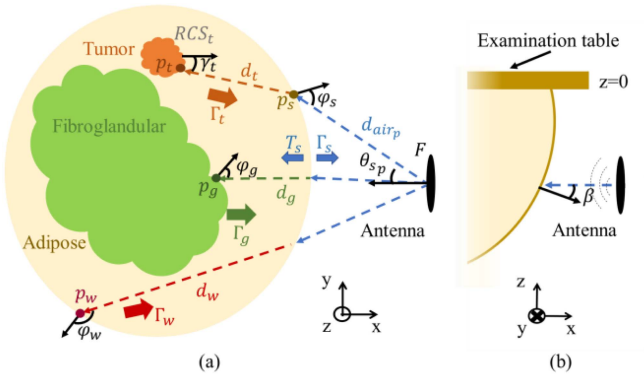


Fig. 1. Ray tracing method applied in this method: (a) Plane XY. (b) Plane XZ.

$$s_{11}\ (f) = \Gamma_a\ (f) + b_s\,(f) + b_g\,(f) + b_t\,(f) + b_w\,(f) + \eta \tag{1}$$

Depending on the VNA characteristics and on the above parameter configuration, the noise floor can be further reduced (e.g., to -100 dB) eventually with impact on the frequency sweep time and total measurement time.

The return ray path for backscatter is the same as the transmitted ray path. Only first-order reflections are considered. Higher order reflections inside the breast are highly attenuated, and those outside the breast are gated by time domain separation.

We discuss the formulation and implied physical phenomena as we go through one typical ray path. The method is developed for individual 2D *xy*-cuts, however it takes into account some information from the *z*-dimension, such as breast surface slopes and the full 3D structure of the tumor.

The breast profile in the *xy*-plane is discretized into N_s points. We assume that, for each position of the antenna, the received $b_s(f)$ signal is the integral of the individual contribution from all $\subseteq N_s$elementary surfaces of the breast that are illuminated by the antenna, in the physical optics sense.

Consider one of these incident rays from the antenna entering the air-breast interface at a given point p_s at a distance d_{air_p}. We assume a spherical wave radiating from the antenna phase center, $e^{-jk_0(f)d_{air_p}}/d_{air_p}$, where $k_0(f)$ is the free-space wavenumber at frequency f. Although these concepts are not strictly applicable in a near-field type scenario, this is a reasonable approximation discussed at length in [22]. The wave suffers a major reflection/scattering at this boundary, with much lower transmission level into the breast tissues. We need to analyze both.

The back-scattered signal $b_s(f)$ at the air-breast interface is determined by the breast scattering cross-section σ_s, which depends on the surface main local radius of curvature (ρ_{xy}, ρ_z) and slopes (∂_{xy}, ∂_z), incidence angle and dielectric contrast.

Full-wave computation of the breast radar cross section for all possible incidence angles is computationally intensive, not compatible with the desired very fast breast response generation. Therefore, given that the breast shape is smooth, with very slow dependence on coordinates, we use physical reasoning to establish an alternative approximate, faster representation of the breast skin back-scattered signal $b_s(f)$ that is received at the antenna

$$b_s\ (f) = c_s \sum_{p\ =ps_i}^{ps_f} \frac{F\left(\theta_{sp}\right)}{{d_{air}}_p{}^2} \sqrt{\sigma_s\left(f,\ \varphi_s, \beta\right)} \times e^{-2jk_0(f)d_{air_p}} \tag{2}$$

where the sum is extended to the $\boldsymbol{ps_i}$ to $\boldsymbol{ps_f}$ subset of the breast perimeter points that are visible to the antenna. Function $\boldsymbol{\sigma_s}(\boldsymbol{\varphi_s}, \boldsymbol{\beta})$ is the breast's external boundary radar cross-section (RCS), $\boldsymbol{\varphi_s}, \boldsymbol{\beta}$ are the local incidence angles in the main planes defined in Fig. 1. The antenna is represented by its radiation power pattern $\boldsymbol{F}(\boldsymbol{\theta_{sp}})$ and by the phase center, instead of modeling the physical structure. This accelerates the computation and does not prevent agreements between measurements and the model's results, as will be seen ahead. The factor $\boldsymbol{c_s}$ is a calibration constant to be set later, in the calibration measurements. The breast external boundary RCS is approximated as:

$$\sigma_s\left(f, \varphi_s, \beta\right) \approx \left(\left|\Gamma_s\left(f\right)\right| \cos\varphi_s \cos\beta\ \right)^2 \|t_s\|\ \rho_z \tag{3}$$

where $\Gamma_s\ (f) = (n_s(f) - 1)/(n_s(f) + 1)$ is the reflection coefficient, and n_s is the dispersive refraction index of the adipose tissue. The product $\|t_s\|\ \rho_z$ gives an approximate area of the elementary surface of the breast, where the first factor is the distance between two consecutive points of the breast perimeter, and the second factor is the surface curvature radius in the vertical plane (in practice replaced by ρ_{xy}). While part of the incident energy is scattered back to the antenna, the other part enters the breast according to Snell's law. The transmitted rays may reach the tumor's surface, or the fibroglandular surface, or the breast back wall. The tumor's contribution to $s_{11}(f)$, if reached by the incident wave, becomes:

$$b_t\ (f) = c_t \sum_{p\ =\ pt_i}^{pt_f} \frac{F\left(\theta_{sp}\right)}{{d_{air}}_p{}^2} \left|T_s\left(f\right)\right|^2 \cos\varphi_s \cos\beta \sqrt{\sigma_t\left(f, \gamma_t\right)} \times e^{-2jk_0(f)\cdot\left(d_{air_p} + n_s(f)d_t\right)} \tag{4}$$

where the sum is extended to all pt_i to pt_f points from the N_s set that hit the visible tumor boundary. These points are determined by ray tracing. Function $T_s\left(f\right) = 2\,n_s(f)/(1 + n_s(f))$ is the Fresnel transmission coefficient calculated at the breast-air boundary. Factor c_t is a calibration coefficient to be set with the calibration measurement.

Function σ_t is the full-wave radar cross section $RCS_t(f, \gamma_t)$ of the tumor. It is pre-calculated using the "rcs" built-in MatLab function [23], which calculates the RCS of a 3D metal object in air. To obtain the RCS of the tumor in a background medium with permittivity ε_r, we scale up the tumor size by $\sqrt{\varepsilon_r}$; the result $RCS^{air}_{scaled}(f, \gamma_t)$ is then divided by ε_r to obtain the RCS of a metal tumor of the original size surrounded by the ε_r media. This

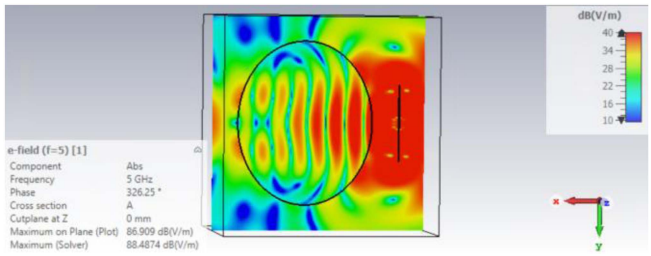


Fig. 2. Two-dimensional cut of the E-field at 5 GHz of a simulation in CST [24] containing an antenna radiating a typical breast with permittivity of 5 and loss tangent of 0.1.

equivalence was verified by full-wave calculation. To account for the effect of the tumor dielectric material, the result is multiplied, as an approximation, by the Fresnel reflection coefficient:

$$RCS_t\ (f, \gamma_t) = \frac{RCS^{air}_{scaled}\left(f, \gamma_t\right)}{\varepsilon_r} \Gamma_t(f)^2 \tag{5}$$

with $\Gamma_t\ (f) = (n_t(f) - n_s(f))/(n_t(f) + n_s(f))$, where n_t is the dispersive refractive index of the tumor tissue.

Note that the wavefront of the transmitted wave tends to become planar for the usual values of the adipose tissue permittivity, due to refraction at the curved boundary; therefore, in (4) we drop the inverse distance dependence inside the breast. As an example, and to show this effect, we depict in Fig. 2, a two-dimensional cut of the electrical field of a simulation with a breast with typical dielectric properties (permittivity of 5 and loss tangent of 0.1) radiated by an antenna, at $f = 5$ GHz. This is a full-wave simulation performed on the Computer Simulation Technology (CST) Microwave Transient Solver [24].

The phase term includes the phase shift corresponding to the go and return propagation over the d_t distance in the adipose tissue.

As for the rays hitting the fibroglandular boundary or the inside of the backwall, the contribution for $s_{11}(f)$is calculated from a similar expression:

$$b_k\ (f) = c_k \sum_{p\ =\ pk_i}^{pk_f} \frac{F\left(\theta_{sp}\right)}{{d_{air}}_p{}^2} \left|T_s\left(f\right)\right|^2 \cos\varphi_s \cos\beta \sqrt{\sigma_k\left(f, \varphi_k\right)} \times e^{-2jk_0(f)\cdot\left(d_{air_p} + n_s(f)d_k\right)} \tag{6}$$

where index k can be either g for the fibroglandular tissues or w for the back wall. The sum in (6) is extended to all pk_i to pk_f points from the $N_s$set that hit the visible fibroglandular boundary, or the visible part of the back wall. The equation for the cross section σ_k is like (3), changing appropriately the refractive index of the media materials and dimensions involved:

$$\sigma_k\left(f, \varphi_i\right) \approx \left(\left|\Gamma_k\left(f\right)\right| \cos\varphi_k\right)^2 \|t_k\|\ \rho_z \tag{7}$$

with $\Gamma_g\ (f) = (n_g(f) - n_s(f))/(n_g(f) + n_s(f))$, where $n_g(f)$ is the refraction index of the fibroglandular tissue, and $\Gamma_w\ (f) = (1 - n_s(f))/(1 + n_s(f))$ for the back wall case. Again, the product $\|t_k\|\ \rho_z$ is the contributing elementary area. Finally, as before, the calibration coefficient c_k is to be set in the calibration measurements.

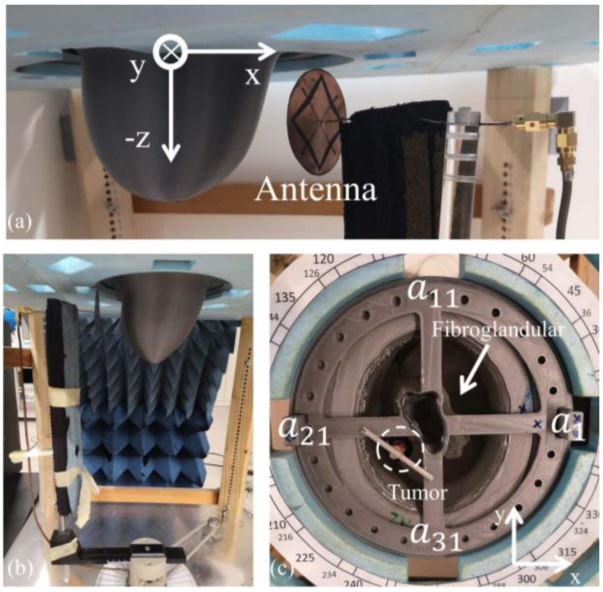


Fig. 3. Experimental setup: (a) Antenna XETS directed to a breast phantom placed in a Styrofoam base. (b) Overview of the setup with antenna connected to a rotary arm, which is in turn connected to a vector network analyzer. (c) Top view of a heterogeneous breast phantom with antenna position information.

III. Experimental Setup

This section describes the experimental MW setup used to validate the digital twin, as well as the fabrication of breast and tumors phantoms employed in this work.

A. Microwave Imaging Setup

The experimental set-up that we used for the development and test of its digital twin is an air-operated MW breast scanning system developed at Instituto de Telecomunicações [4] (Fig. 3). It represents part of an exam table, where patients would lie in prone position, with the breast pending through a circular opening. The antenna is mounted below the table and can scan around the breast. It is connected to an ENA Series Network Analyzer Agilent E5071C, through a rotary joint, to avoid cable torsion or bending that might otherwise introduce amplitude and phase uncertainties. The numbering of the antenna positions is indicated in Fig. 2.

The used antenna was a crossed exponentially tapered slot-based (XETS) antenna [22], calibrated with a Keysight Electronic Calibration device (E-cal); the radius of the antenna scanning path was 90 mm, and data was collected at 9° angular intervals (40 positions) for the 2 to 5 GHz frequency range (151 frequency points). The selected number of frequency points and the used bandwidth imply that the aliasing distance is greater than 7 m. At such distances, any scattering contributions from the laboratory environment are extremely weak and effectively negligible compared to the first-order reflections originating within the breast. This ensures that no spurious external scattering folds back into the breast domain. Those existing for smaller distances are time-gated. In each scan, a tumor was placed in different fixed positions inside the breast and kept in the same z-plane plane as the antenna (at $z = -35$ mm).

In the first stage, we collected the responses of homogeneous breast phantoms, i.e., breasts composed of adipose tissue only (no fibroglandular tissue), and then evolved to heterogeneous breasts phantoms, i.e., breasts with adipose and fibroglandular tissues. For each breast type, we considered initially breasts with regular shapes (cylindrical and elliptical shape), and later anthropomorphic ones. The canonical shapes steps were essential to tune the model's four calibration coefficients c_s, c_t, c_b, c_w of *MWSensing*.

Measurement protocol was performed as follows (remember one measurement scenario involves 40 antenna positions):

1) *Free-space* (without breast: 40).
2) *Two canonical breast shells:*
   a) Homogeneous (with tumor at two positions, one at a time: 160).
   b) Heterogeneous (with one fibroglandular shell: 80; with one fibroglandular shell and tumor at two positions, one at a time: 160).
   c) Control (without fibroglandular and tumor: 80).

In total, we took 480 measurements.

a) *Two anthropomorphic breast shells:*
   a) Homogeneous (with tumor at two positions: 160).
   b) Heterogeneous (with two fibroglandular shells, one at the time: 160; with two fibroglandular shells, one at a time, and tumor at two positions: 320).
   c) Control (without fibroglandular and tumor: 80).

In total, we took 720 measurements.

B. Fabrication of Breast Phantoms and Tumors

The breast phantoms comprise the skin and fibroglandular shells, as well as the liquid mixtures that fill these containers to mimic the electromagnetic response of the adipose, fibroglandular, and the tumor.

All shells were 3D-printed with 1.2 mm wall-thick polylactic acid (PLA, $\varepsilon_r = 2.75 - j0.03$ at 4 GHz [25]), using a Ultimaker 3 Extended printer [26]. Although PLA does not represent the actual dielectric properties of the skin, it was shown in [4] that this approximation does not change the nature of MW signals, just its magnitude response. On the same token, PLA was used to fabricate the fibroglandular shell, as in [5] and [13].The implied response amplitude differences can be compensated with proper adjustment of the method's calibration coefficients. Fig. 4 shows the 3D-printed shells used in this study, along with the respective volumes in mm^3.

The anthropomorphic breasts A2 and A12, and the fibroglandular containers F2, F3, and F4 reproduce MRI-derived breast models from the University of Manitoba repository [13]. This repository is accepted in the literature as fair representations of actual breast shapes. To represent an initial smaller and simpler fibroglandular container for the calibration phase, an 80% scaled down version of F4 was produced, labeled F4s.

Breast containers were filled with TX-100, which approximates the dielectric properties of adipose tissue, presenting a measured permittivity of $4.1 - j0.7$ at 4 GHz, while fibroglandular containers were filled with a mixture of TX-100, distilled water and sodium chloride (NaCl) which presented a measured permittivity of $31.2 - j12.0$ at 4 GHz. The recipes

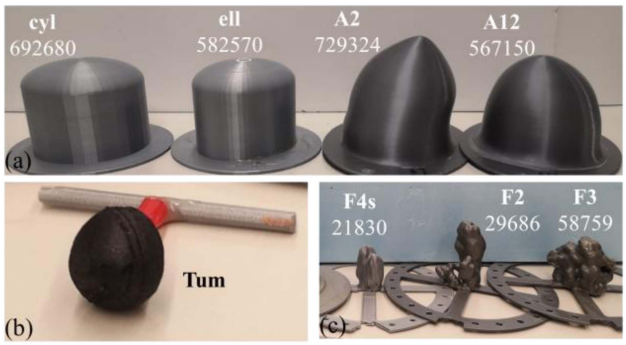


Fig. 4. 3D-printed breast and fibroglandular containers, with respective volumes in mm^3, and the carbon-black tumor used in this work (a) Breast Cylindrical, Elliptical, A2, A12 (b) Tumor (c) Fibroglandular F4s, F2, F3.

for the liquids inside each type of container were retrieved from [27], and are accepted as good approximations of the biological tissues.

Lastly, the tumor shape (Fig. 4) was generated using the Gaussian Random Sphere model (GRS) [28]. Again, this is common practice in breast modelling literature [9]. The tumors were built with 10-mm average radius using a mixture of polyurethane, carbon black, graphite, and acetone [12]. The measured permittivity was $43.0 - j14.3$ at 4 GHz.

IV. Method Validation

For validation, we need to numerically implement the proposed method, define evaluation metrics along with the calibration protocol, and then compare the model results with equivalent measured results for several representative cases.

A. Numerical Implementation

A code was developed in MatLab – *MWSensing* – according to the formulation presented in Section II. It has a user-friendly graphical interface that allows generating, or loading and visualizing different tumor and breast profiles, specifying different tissue characteristics for the adipose, fibroglandular, and tumor tissues. These properties can be chosen to be constant or follow a Cole-Cole model within a specified range of frequencies.

Tumors can be internally generated with different morphologies to represent different levels of malignancy, a feature that is of great importance when trying to improve the effectiveness of MW algorithms for detection of breast cancer. To this end, we have the option to generate smooth (benign) or parametrized spiculated (malignant) tumors. For spiculated tumors, the user can choose the number of spikes and their size, mimicking the level of malignancy of the tumor. Once the shape is defined, its RCS is pre-calculated for all incidence angles and stored in a look-up table.

It is also possible to define the number N_a of antenna positions in a circular path around the breast, with user-defined radius. The antenna positions are considered independently, as if a single antenna was scanned around the breast; therefore, the code does not need to consider mutual coupling among antennas. Extension of the proposed rationale to multi static arrays would require modeling the antennas' mutual coupling effects, implementing the s_{ij} terms, and computing and storing the multi-static RCS of the tumor for all antennas and frequencies. This would increase significantly the computational time. This generalization lies beyond the scope of the present work.

Furthermore, since the $\Gamma_a(f)$term in (1) can be easily removed from experimental or full-wave simulated results, and in fact it has to be removed for proper image inversion, we do not include it in this model. The magnitude of the radiation pattern of a real antenna is employed in $F(\theta_{sp})$.

The code output is a collection of generated $s_{11}(f)$ files corresponding to a user defined list of different conditions that are analyzed as a batch. The code allows to output the separate scattering contributions from each element of the breast (each term or combination of terms from (1)), if needed for verification, or calibration. After finishing the simulation, the files in s1p format can be exported. On average, the $s_{11}(f)$ calculation may take approximately 6 milliseconds per antenna and per frequency point, using an Intel(R) Core (TM) i7-8565U CPU at 1.8 GHz with 16 GB RAM.

In this work, simulation conditions—including frequency band, dielectric properties, breast geometries, and tumor placements—were aligned with the experimental setup to ensure direct comparability between measured responses and the digital twin responses.

The features implemented in *MWSensing* are much more general than what is needed for the current paper. The full-featured executable code representing the digital twin of our laboratory setup is openly available in [18].

B. Signal Processing and Performance Metrics

The model assessment is based on metrics that allow comparing images inverted from *MWSensing* results and from experimental results.

For that, the raw $s_{11}(f)$ is pre-processed, starting by subtracting the antenna free space input reflection, to remove $\Gamma_a(f)$. This step is not needed for the digital twin responses, because Γ_a is not included from the start, as mentioned.

Then, we remove the skin artifact – the very intense backscatter from the skin. In this paper, we use two alternative approaches to remove skin artifacts. The first is based on an Ideal Calibration (IC). For a low-density breast, represented by a homogenous breast containing just adipose tissue and tumor, we have:

$$b_t\ (f) = s_{11}\ (f) - s_{11}^{t}(f) \tag{8}$$

where the superscript notation stands for the removed scattering terms: the second term on the right-hand side indicates that the calculated or measured s_{11} are obtained without considering the tumor. For heterogeneous breasts:

$$b_t(f) + b_g\ (f) = s_{11}\ (f) - s_{11}^{g,\,t}(f) \tag{9}$$

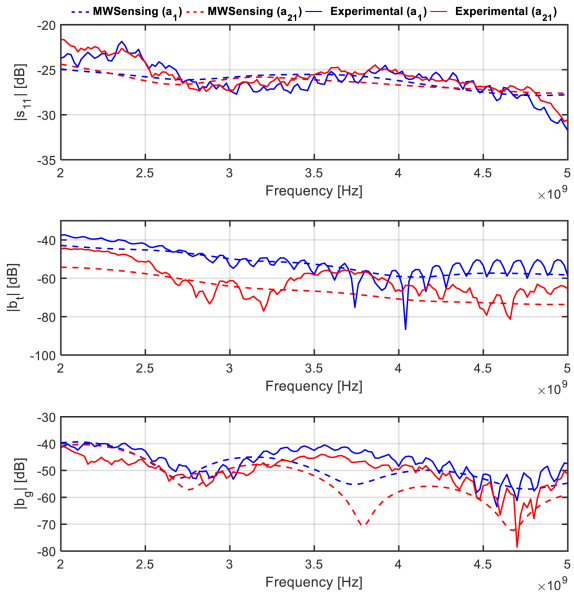


Fig. 5. Magnitude responses, in dB, of two distinctive antennas positions a_1 and a_{21}obtained using cylindrical breast shell and F4s fibroglandular model with tumor at position (25, 20, -35) mm: (a) total signal response $s_{11}(f)$ (b) tumor signal response $b_t(f)$ (c) fibroglandular signal response $b_g(f)$.

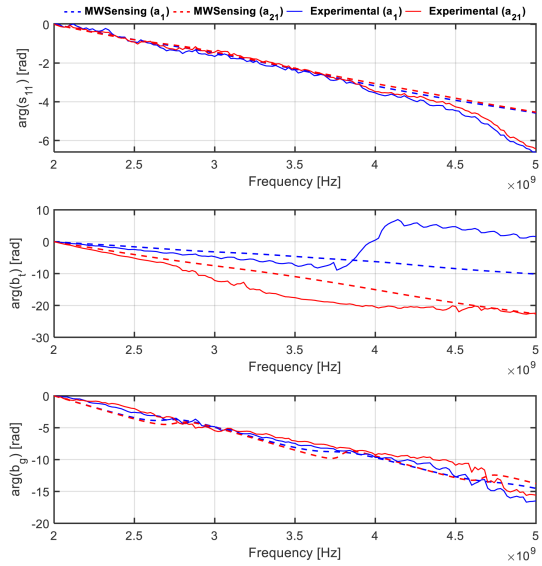


Fig. 6. Phase responses, in radians, for two different antenna positions a_1 and a_{21}near cylindrical breast shell and F4s fibroglandular model with the tumor in position (25, 20, -35) mm: (a) total signal response $s_{11}(f)$ (b) tumor signal response $b_t(f)$ (c) fibroglandular signal response $b_g(f)$.

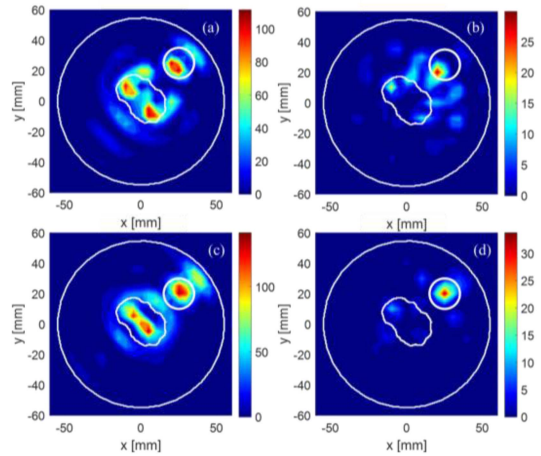


Fig. 7. Two-dimensional numerical images obtained considering N_a= 40, f = 2-5 GHz and $n_s(4\,GHz)$ = 4.1-j0.7, using cylindrical breast shell and F4s fibroglandular model with the tumor at position (25, 20, -35) mm: (a) Experimental with IC (b) Experimental with SVD (c) *MWSensing* with IC (d) *MWSensing* with SVD. The outer white contour represents the breast shape in the z-plane in which the antenna and tumor are placed; the circular and smaller contour represents the tumor, and the irregular one identifies the shape of the fibroglandular tissue.

Although this method is not feasible with signals measured on real patients, it can be done in the laboratory or in simulations, to provide better insight into the best detection possibility. The alternative artifact removal algorithm we use, which is applicable in real patients' data, is based on singular value decomposition (SVD) [4]. This method decomposes the scattered response into a set of contributions separated and ranked by their received power and scatterer distance, allowing an effective removal of the first and strongest response originated by the breast skin, leading to the filtered response.

After removing the response of the skin from the signals, obtaining s_{11}^{cal}, we use the Kirkhoff Migration algorithm, which combines confocally the s_{11}^{cal} values obtained for all antenna positions, to calculate the scattered intensity I for each pixel with coordinates $(x, y)$of the inversion image.

$$I\,(x,y) = \sum_{a=1}^{N_a} \sum_{f=f_{\min}}^{f_{\max}} s_{11}^{cal}\,(a,f)\, e^{2jk_0(f)\left(d_b n_s(f) + d_{air_p}\right)} \quad (10)$$

where d_b is the distance travelled inside the breast until the correspondent pixel. The input parameters used in this process are compatible with the experimental setup, i.e $N_a = 40$, $f_{\min} = 2\,GHz$, $f_{\max} = 5\,GHz$, $n_s(f)$ varies and is $4.1 - j0.7$ for 4 GHz.

To assess the quality of each image, we use quantitative metrics:

1) *Tumor-to-clutter ratio (TCR):* compares the maximum scattered intensity corresponding to the tumor response ($\boldsymbol{I_T}$) and the larger unwanted artifact intensity (clutter - $\boldsymbol{I_C}$), occurring in the 2D image:

$$TCR\ [dB] = 10\log_{10}\frac{\max\,(I_T)}{\max\,(\mathrm{I_C})} \quad (11)$$

The second metric provides a measure of the image similarity between computed and measured results:

2) *Mean-Squared Error (MSE):* first, all $\boldsymbol{N_{px}}$ pixels are normalized to the maximum value of the intensity in each of the two images; then, the squared difference between matching pairs of pixels from both images is averaged:

$$MSE\ [\%] = \frac{\sum_{px=1}^{N_{px}} \left[I^{MWSensing}\,(px) - I^{Experimental}\,(px)\right]^2}{N_{px}} \times 100 \quad (12)$$

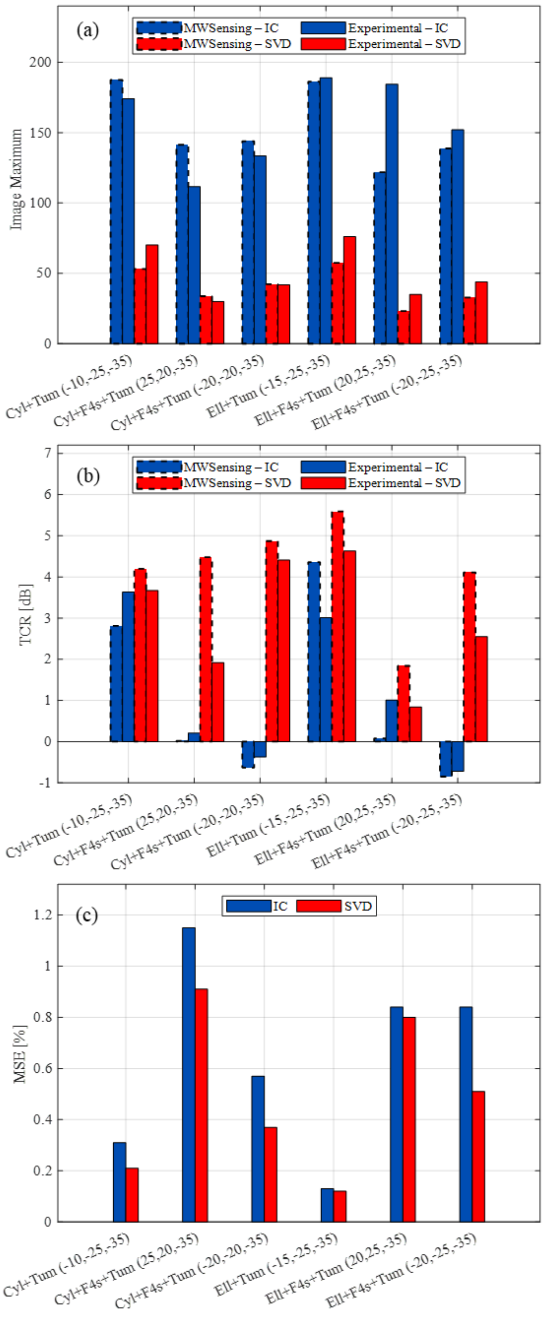


Fig. 8. Quantitative metric results for model calibration in homogeneous and heterogeneous breast scenarios, using cylindrical and elliptical breasts, F4s fibroglandular shell and tumor in different positions: (a) Image Maximum (b) TCR (c) MSE.

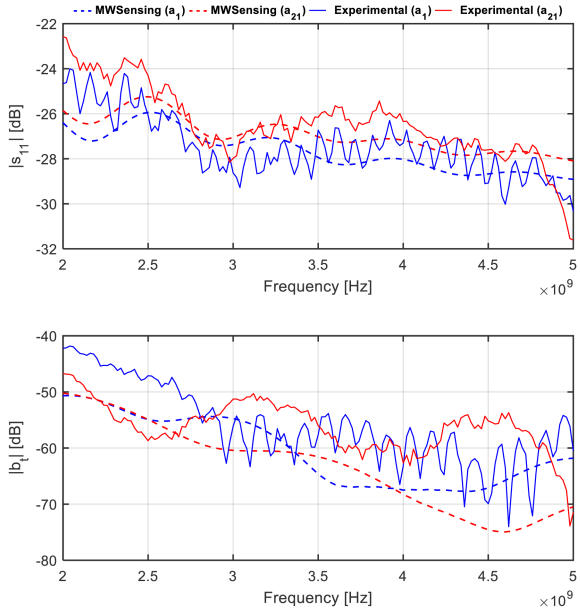


Fig. 9. Magnitude responses, in dB, at two different antenna positions a_1 and a_{21} obtained for A2 breast shell with tumor in position (15,30, -35) mm: (a) total signal response $s_{11}(f)$ (b) tumor signal response $b_t(f)$.

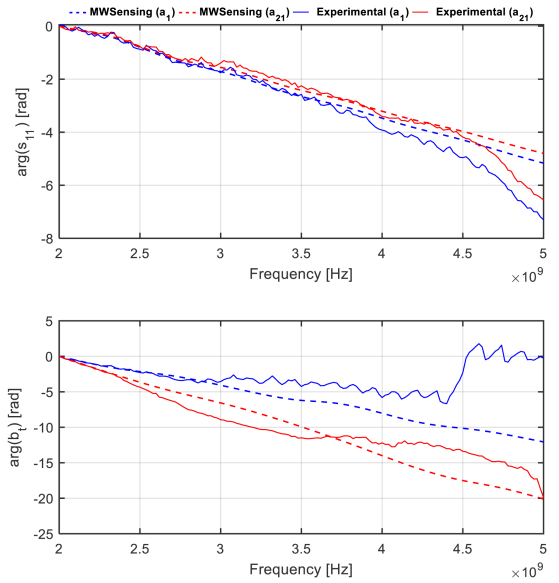


Fig. 10. Phase responses, in radians, at two different antenna positions a_1 and a_{21} obtained for A2 breast shell with tumor in position (15,30, -35) mm: (a) total signal response $s_{11}(f)$ (b) tumor signal response $b_t(f)$.

MSE tends to 0 as the similarity between images increases. This metric represents the percentage difference between images.

C. Model Calibration

We recall that the proposed model contains four calibration coefficients (c_s, c_t, c_g, c_w), that need to be set using reference measurements to incorporate specific effects from the setup, which are not easy to account for in the analytical model. For this adjustment we used canonical breast shapes, (cylindrical and elliptical), a simpler fibroglandular tissue (F4s), and the tumor. The rationale was to compare and match *MWSensing* results with measured signals scattered separately by the breast boundary, by the fibroglandular boundary, and by the tumor. Separate responses are obtained by subtracting measurements with and without the fibroglandular or tumor phantoms. The analysis was carried both in frequency and time (distance) domains. Once set, these coefficients are expected to work well enough for unseen breasts.

We started with homogeneous breasts i.e., without the fibroglandular phantom and established an initial range for coefficients

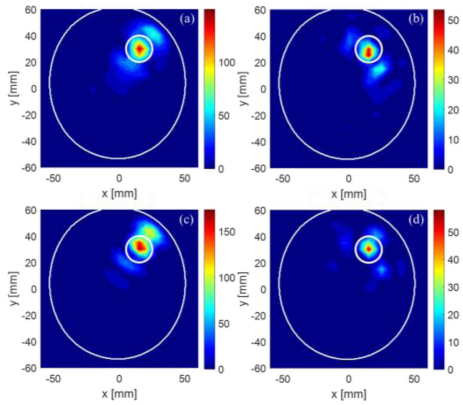


Fig. 11. Two-dimensional numerical images obtained considering $N_a = 40$, f = 2-5 GHz and $n_s(4\,GHz) = 4.1\text{-}j0.7$, using A2 breast shell with tumor at position (15, 30, -35) mm: (a) Experimental with IC (b) Experimental with SVD (c) *MWSensing* with IC (d) *MWSensing* with SVD. The outer white contour represents the breast shape in the z-plane in which the antenna and tumor are placed; the circular and smaller contour represents the tumor.

c_s, c_t, c_w by visual matching the results. An example of the scattered signals in frequency domain is presented in Fig. 5 (magnitude) and Fig. 6 (phase) for the a_1 and a_{21} antenna positions. A non-insertable device used in the port calibration process, slightly impacted the measured frequency response, by introducing a small ripple. Although this ripple is visible in the measured data, it does not have a noticeable impact on the reconstructed images, as its contribution is spread in time and falls outside the imaging domain. The corresponding representation in the distance domain is not shown for conciseness. The matching of all curves is qualitatively good, with similar frequency behavior and proper peak alignment in the distance domain (the latter not shown). The process was repeated to determine a range for the c_g coefficient, using a heterogeneous breast, i.e., with the F4s fibroglandular structure included.

The final tuning of the four coefficients was obtained by optimizing the quantitative TCR and MSE metrics applied to the reconstructed images. These are shown in Fig. 7 for an heterogeneous cylindrical breast, after optimizing the coefficients: $c_s = 6.0 \times 10^{-4}$, $c_t = 1.8 \times 10^{-5}$, $c_g = 9.7 \times 10^{-5}$, $c_w = 8.8 \times 10^{-5}$. The figure compares the results obtained with *MWSensing* with the experimental ones, when the ideal calibration is used (IC) for skin artifact removal, or singular value decomposition (SVD). Fig. 8 shows the quantitative metrics results obtained in the calibration process, considering different tested breast configurations. We highlight the consistency of *MWSensing*'s results against the experimental ones, with very low MSE ($<$1.2%) and good TCR. This confirms that the four weight coefficients are enough to obtain acceptable agreement between the model and these experiments.

V. Results

A. Homogeneous Anthropomorphic Breast Results

After adjusting the settings, we put the digital twin to the test with other different breast configurations, starting with homogeneous anthropomorphic ones. We compare in Figs. 9, 10 and 11 the magnitude and phase responses, as well as image

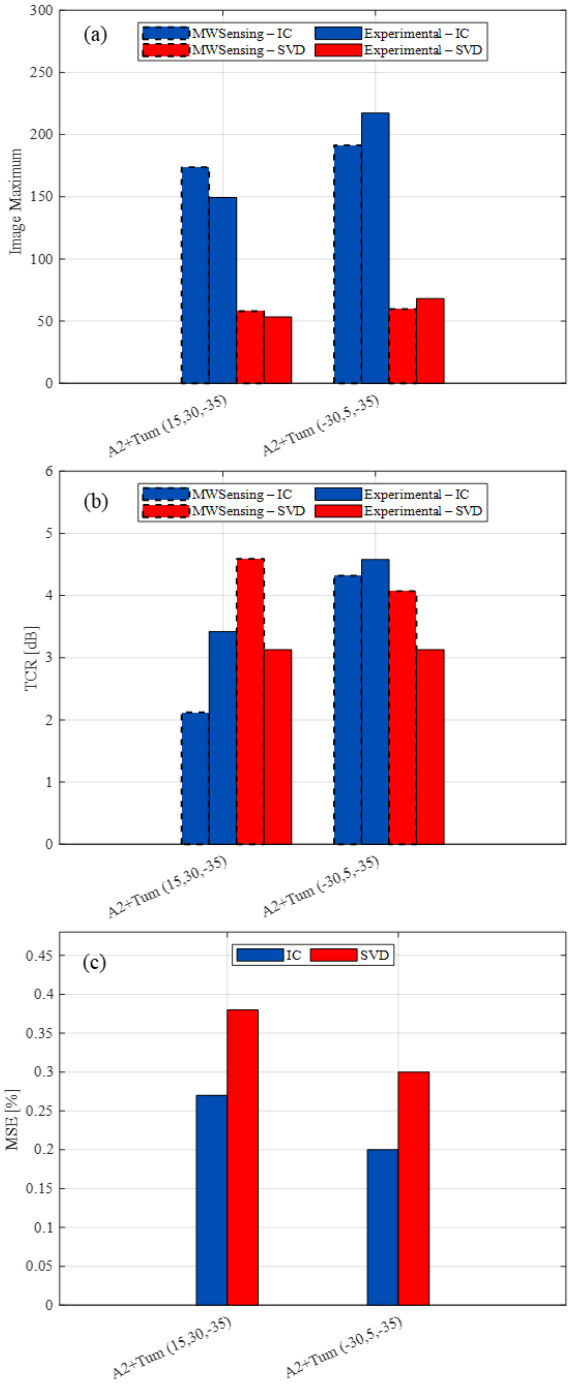


Fig. 12. Quantitative metric results for realistic homogeneous breast scenarios, using A2 breast and tumor in different positions: (a) Image Maximum (b) TCR (c) MSE.

reconstruction results, respectively, for the anthropomorphic breast A2, with homogeneous filling, and one tumor in position $(15,\ 30,\ -35)$ mm inside the breast.

In addition, we present in Fig. 12 the corresponding quantitative metrics for this and for an additional configuration.

Analysis of Fig. 9 show slight differences between the frequency response curves from the simulator and the experimental ones, however, they are of the same nature for both antennas, with similar magnitude range. Phase results in Fig. 10, show

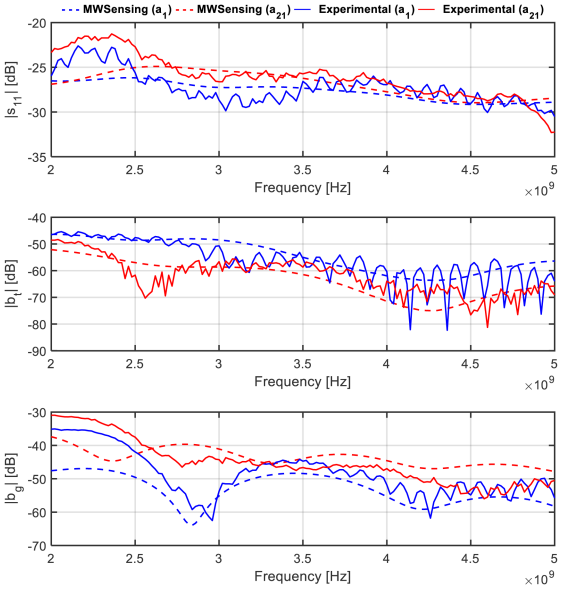


Fig. 13. Magnitude responses, in dB, of two distinctive antennas positions a_1 and a_{21} obtained using A2 breast shell and F2 fibroglandular model with tumor in position (15,-20,-35) mm: (a) total signal response $s_{11}(f)$ (b) tumor signal response $b_t(f)$ (c) fibroglandular signal response $b_g(f)$.

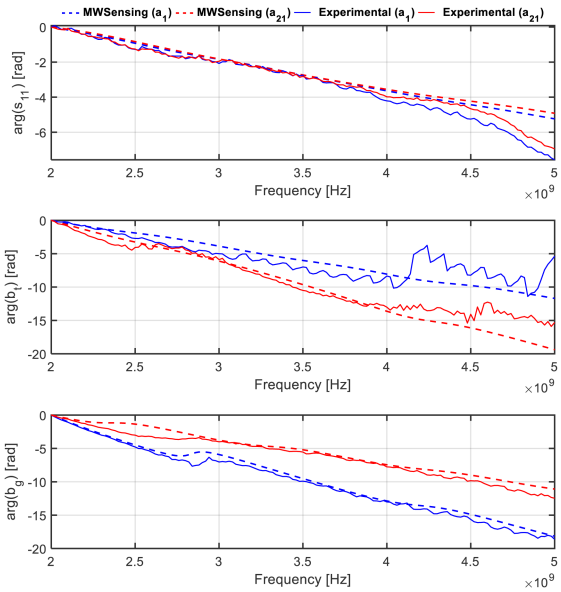


Fig. 14. Phase responses, in radians, of two distinctive antennas positions a_1 and a_{21} obtained using A2 breast shell and F2 fibroglandular model with tumor in position (15,-20,-35) mm: (a) total signal response $s_{11}(f)$ (b) tumor signal response $b_t(f)$ (c) fibroglandular signal response $b_g(f)$.

some differences for $b_t(f)$, especially for increasing frequencies; however, metrics in Fig. 12 show no impact on the quality of the reconstructed image. The phase jumps correspond just to phase unwrapping errors, not to intrinsic phase discrepancies.

The reconstructed images in Fig. 9 identify the tumor correctly with comparable TCR values. Artifacts appear only close to the tumor and are consistent between *MWSensing* and experimental results. Quantitative MSE values are low as desired, and also consistent between the digital twin and experiment.

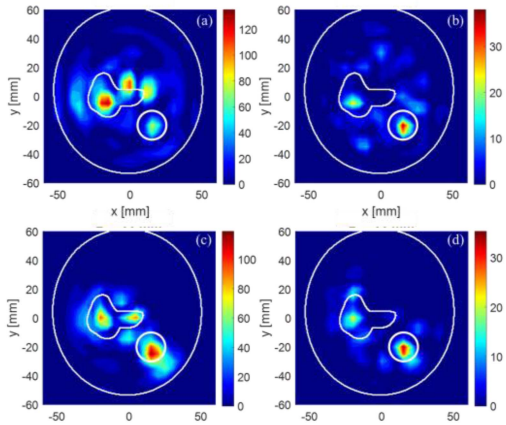


Fig. 15. Two-dimensional numerical images obtained considering $N_a = 40$, f = 2-5 GHz and $n_s(4\,GHz) = 4.1\text{-}j0.7$, using A2 breast shell and F2 fibroglandular model with tumor at position (15, -20, -35) mm: (a) Experimental with IC (b) Experimental with SVD (c) MWSensing with IC (d) MWSensing with SVD. The outer white contour represents the breast shape in the z-plane in which the antenna and tumor are placed; the circular and smaller contour represents the tumor, and the irregular one identifies the shape of the fibroglandular tissue.

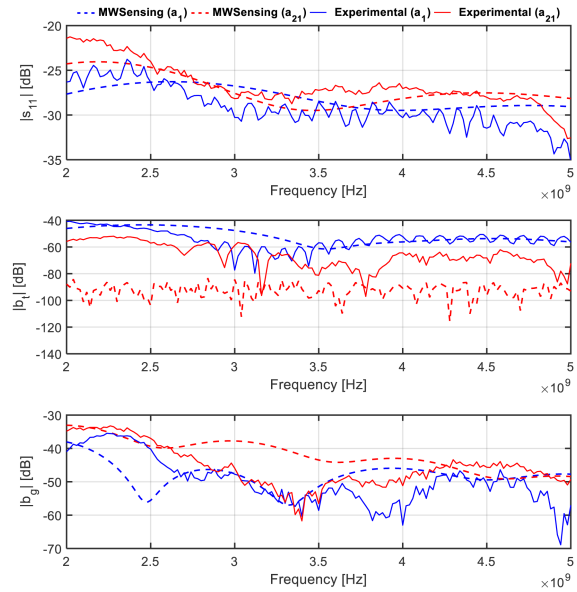


Fig. 16. Magnitude responses, in dB, of two distinctive antennas positions a_1 and a_{21} obtained using A12 breast shell and F3 fibroglandular model with tumor in position (20,25,-35) mm: (a) total signal response $s_{11}(f)$ (b) tumor signal response $b_t(f)$ (c) fibroglandular signal response $b_g(f)$.

B. *Heterogeneous Anthropomorphic Breast Results*

In this section we analyze two different anthropomorphic breast phantoms: the first (A2) presents an elliptical cross-section, while the second (A12) has a circular shape. We consider different fibroglandular models inside each breast, with different shapes (F2 and F3). The magnitude and phase responses, and the corresponding reconstructed images are presented in Figs. 13, 14 and 15, respectively, for breast A2, and in Figs. 16, 17 and 18, for breast A12. The calculated metrics are presented in Fig. 19.

As before, the magnitudes of the frequency response in the simulated and experimental results in Fig. 13 are in the

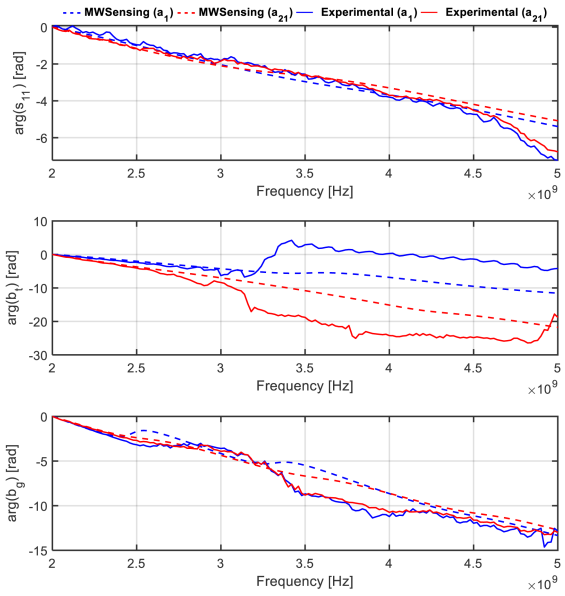


Fig. 17. Phase responses, in radians, of two distinctive antennas positions a_1 and a_{21} obtained using A12 breast shell and F3 fibroglandular model with tumor in position (20,25,-35) mm: (a) total signal response $s_{11}(f)$ (b) tumor signal response $b_t(f)$ (c) fibroglandular signal response $b_g(f)$.

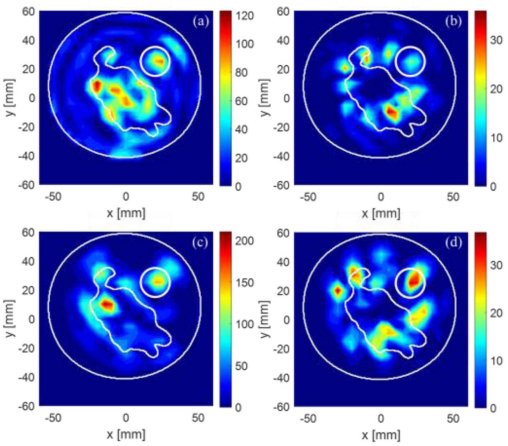


Fig. 18. Two-dimensional numerical images obtained considering $N_a = 40$, f = 2-5 GHz and $n_s(4\,GHz) = 4.1\text{-}j0.7$, using A12 breast shell and F3 fibroglandular model with tumor at position (20,25, -35) mm: (a) Experimental with IC (b) Experimental with SVD (c) MWSensing with IC (d) MWSensing with SVD. The outer white contour represents the breast shape in the z-plane in which the antenna and tumor are placed; the circular and smaller contour represents the tumor, and the irregular one identifies the shape of the fibroglandular tissue.

same magnitude range. The trend of the phase results, obtained from $s_{11}(f)$ and $b_t(f)$ is quite like in the homogeneous test. The difference in $b_g(f)$ is expected and inevitable since *MWSensing* only considers first order interactions.

The reconstructed images using the IC skin artifact removal (Fig. 15(a) and (c)) present some other artifacts, but even so very comparable results between *MWSensing* and experiment. The SVD images also present artifacts, originating from the fibroglandular tissue, even so very consistent between the simulation and experiment.

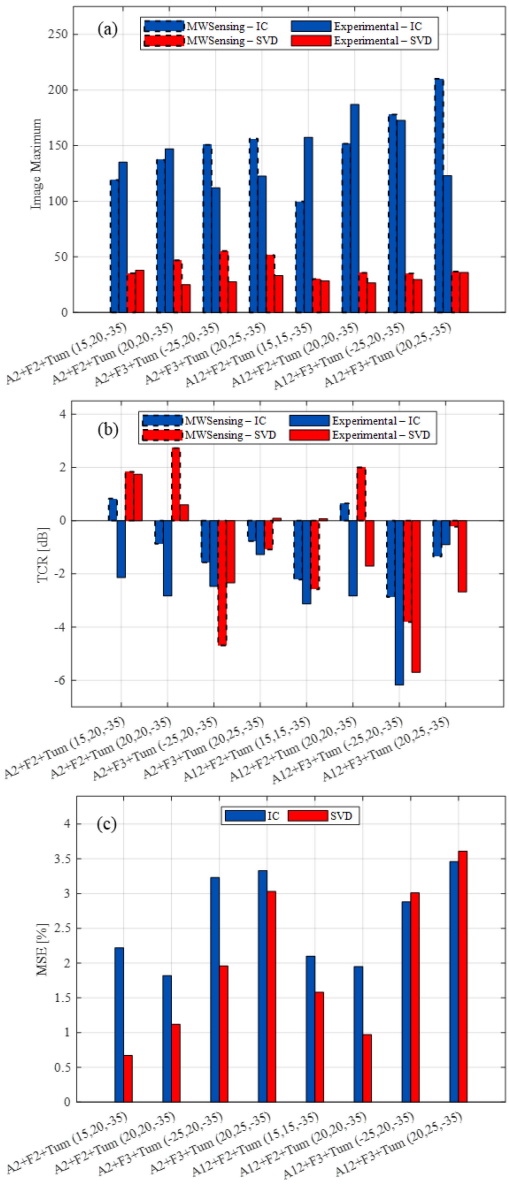


Fig. 19. Quantitative metric results for realistic heterogeneous breast scenarios, using A2 and A12 breasts, F2 and F3 fibroglandular shells and tumor in different positions: (a) Image Maximum (b) TCR (c) MSE.

The second example is more challenging due to the size and complexity of the fibroglandular tissue. We see more pronounced differences between the *MWSensing* and the experimental results (Figs. 16 to 18). This is expected since the fibroglandular tissue occupies a substantial part of the breast and can hide the tumor from certain antennas. This is clear in the $|b_t(f)|$ response for antenna position 21, where the antenna is completely blocked by the fibroglandular tissue. In the experimental case, since the radiation can go through tissues, the radiation emitted by these antenna positions may reach the tumor, but even so very slightly, as is visible in lower frequencies.

Other differences in Fig. 18 are due to multiple bounces between tissues in the experiment, which are not accounted for in

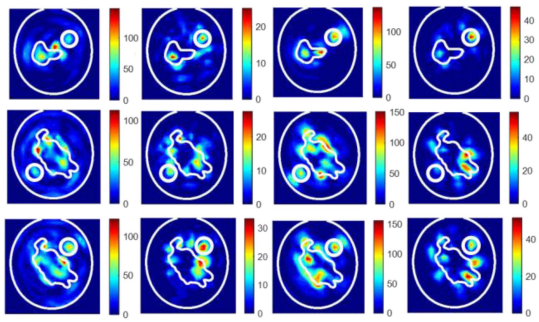


Fig. 20. Two-dimensional numerical images obtained considering $N_a = 40$, f = 2-5 GHz and $n_s(4\,GHz) = 4.1\text{-}j0.7$, using A2 breast shell and F2 and F3 fibroglandular model with tumor at different positions: (1[a] column) Experimental with IC (2[a] column) Experimental with SVD (3[a] column) MWSensing with IC (4[a] column) MWSensing with SVD. Each line represents a different breast configuration, The outer white contour represents the breast shape in the z-plane in which the antenna and tumor are placed; the circular and smaller contour represents the tumor, and the irregular one identifies the shape of the fibroglandular tissue.

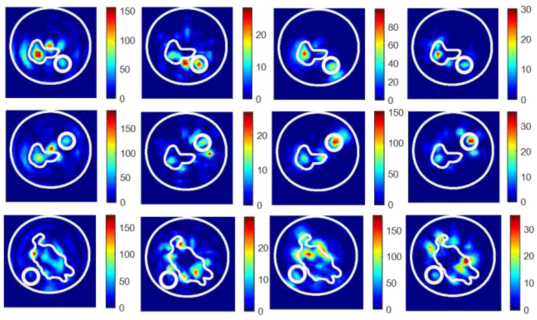


Fig. 21. Two-dimensional numerical images obtained considering $N_a = 40$, f = 2-5 GHz and $n_s(4\,GHz) = 4.1\text{-}j0.7$, using A12 breast shell and F2 and F3 fibroglandular model with tumor at different positions: (1[a] column) Experimental with IC (2[a] column) Experimental with SVD (3[a] column) MWSensing with IC (4[a] column) MWSensing with SVD. The outer white contour represents the breast shape in the z-plane in which the antenna and tumor are placed; the circular and smaller contour represents the tumor, and the irregular one identifies the shape of the fibroglandular tissue.

the adopted first-order reflection model. These effects increase the MSE metric value, but overall, the agreement between the model and the experiment are reasonably good in terms of quantitative metrics. TCR and MSE metrics are compared in Fig. 19 for several other heterogeneous breasts to assess the generality of the proposed model. The respective reconstructed images are presented in Figs. 20 and 21. In all cases, there is consistency between the *MWSensing* and the experimental results, as expected from a digital twin.

VI. Conclusion

This paper proposes a streamlined method to solve the direct problem in breast microwave imaging analysis, based on geometrical optics and physical optics plus full-wave methods, intended for the implementation of digital twins of existing laboratory setups. It can generate massive datasets of realistic backscattering results in a fraction of the time that would be needed by experiment or full-wave simulation. This may be useful for machine learning training or for other types of analysis requiring the evaluation of the sensitivity and specificity of breast cancer detection methods, which require large number of analyzed cases.

This method applies to monostatic air-operated setups. The proposed model incorporates four weight coefficients that must be set to accommodate specific aspects of the adopted measurement setup. We have used this model to implement a digital twin – *MWSensing* – of our experimental laboratory setup, and show throughout the paper the model calibration process, and examples of the obtained results for different combinations of breast phantoms, fibroglandular tissues and tumor positions. The agreement in terms of reconstructed images between laboratory experiment results and the digital twin is evaluated through quantitative metrics, showing satisfactory agreement.

Our tool is made openly available online [18]. Several scenario parameters, like the breast or tumor shape, tissue permittivity, number of antennas to name a few, are configurable by the user. The tool may be useful for the research community that requires large representative datasets of the breast microwave response in a monostatic configuration.

References

[1] P. M. Meaney, M. W. Fanning, D. Li, S. P. Poplack, and K. D. Paulsen, "A clinical prototype for active microwave imaging of the breast," *IEEE Trans. Microw. Theory Techn.*, vol. 48, no. 11, pp. 1841–1853, Nov. 2000.

[2] N. K. Nikolova, "Microwave imaging for breast cancer," *IEEE Microw. Mag.*, vol. 12, no. 7, pp. 78–94, Dec. 2011.

[3] E. C. Fear, J. Bourqui, C. Curtis, D. Mew, B. Docktor, and C. Romano, "Microwave breast imaging with a monostatic radar-based system: A study of application to patients," *IEEE Trans. Microw. Theory Techn.*, vol. 61, no. 5, pp. 2119–2128, May 2013.

[4] J. M. Felício, J. M. Bioucas-Dias, J. R. Costa, and C. A. Fernandes, "Microwave breast imaging using a dry setup," *IEEE Trans. Comput. Imag.*, vol. 6, pp. 167–180, 2020.

[5] R. A. Martins, J. M. Felicio, J. R. Costa, and C. A. Fernandes, "Systematic analysis of microwave breast imaging detection of different-sized malignant and benign tumors," in *Proc. 16th Eur. Conf. Antennas Propag.*, 2022, pp. 1–4.

[6] Q. H. Liu et al., "Active microwave imaging. I. 2-D forward and inverse scattering methods," *IEEE Trans. Microw. Theory Techn.*, vol. 50, no. 1, pp. 123–133, Jan. 2002.

[7] K. Edwards, V. Khoshdel, M. Asefi, J. LoVetri, C. Gilmore, and I. Jeffrey, "A machine learning workflow for tumour detection in breasts using 3D microwave imaging," *Electronics*, vol. 10, no. 6, Mar. 2021, Art. no. 674.

[8] J. Sacristán, B. L. Oliveira, and S. Pistorius, "Classification of electromagnetic signals obtained from microwave scattering over healthy and tumorous breast models," in *Proc. IEEE Can. Conf. Elect. Comput. Eng.*, 2016, pp. 1–5.

[9] S. K. Davis, B. D. Van Veen, S. C. Hagness, and F. Kelcz, "Breast tumor characterization based on ultrawideband microwave backscatter," *IEEE Trans. Biomed. Eng.*, vol. 55, no. 1, pp. 237–246, Jan. 2008.

[10] B. Oliveira, D. Godinho, M. O'Halloran, M. Glavin, E. Jones, and R. C. Conceição, "Diagnosing breast cancer with microwave technology: Remaining challenges and potential solutions with machine learning," *Diagnostics*, vol. 8, no. 2, 2018, Art. no. 36.

[11] M. Lu, X. Xiao, Y. Pang, G. Liu, and H. Lu, "Detection and localization of breast cancer using UWB microwave technology and CNN-LSTM Framework," *IEEE Trans. Microw. Theory Techn.*, vol. 70, no. 11, pp. 5085–5094, Nov. 2022.

[12] B. L. Oliveira, D. O'Loughlin, M. O'Halloran, E. Porter, M. Galvin, and E. Jones, "Microwave breast imaging: Experimental tumour phantoms for the evaluation of new breast cancer diagnosis systems," *Biomed. Phys. Eng. Exp.*, vol. 4, no. 2, 2018, Art. no. 025036.

[13] T. Reimer and S. Pistorius, "The diagnostic performance of machine learning in breast microwave sensing on an experimental dataset," *IEEE J. Electromagnetics, RF Microw. Med. Biol.*, vol. 6, no. 1, pp. 139–145, Mar. 2022.

[14] T. Reimer, J. Krenkevich, and S. Pistorius, "An open access experimental dataset for breast microwave imaging," in *Proc. 14th Eur. Conf. Antennas Propag.*, 2020, pp. 1–5.

[15] R. Sidebottom, D. Webb, B. Bishop, K. Mohammed, and S. Allen, "Results for the London investigation into dielectric scanning of lesions study of the MARIA M6 breast imaging system," *Brit. J. Radiol.*, vol. 97, pp. 549–552, Mar. 2024.
[16] A. Janjic et al., "SAFE: A novel microwave imaging system design for breast cancer screening and early detection—Clinical evaluation," *Diagnostics*, vol. 11, 2021, Art. no. 533.
[17] D. Á. Sánchez-Bayuela et al., "A multicentric, single arm, prospective, stratified clinical investigation to evaluate mammowave's ability in breast lesions detection," *PLoS One*, vol. 18, no. 7, Jul. 2023, Art. no. e0288312.
[18] Instituto de Telecomunicações, "MWSensing Tool," 2025. [Online]. Available: https://www.it.pt/AutomaticPage?id=3489
[19] D. Flores-Tapia, G. Thomas, A. Sabouni, S. Noghanian, and S. Pistorius, "Breast tumor microwave simulator based on a radar signal model," in *Proc. IEEE Int. Symp. Signal Process. Inf. Technol.*, 2006, pp. 17–22.
[20] D. O'Loughlin et al., "Opensource software for microwave radar-based image reconstruction," in *Proc. 12th Eur. Conf. Antennas Propag.*, 2018, pp. 1–4.
[21] D. Kurrant et al., "MWSegEval—An image analysis toolbox for microwave breast images," *SoftwareX*, vol. 15, 2021, Art. no. 100728.
[22] J. M. Felício, J. M. Bioucas-Dias, J. R. Costa, and C. A. Fernandes, "Antenna design and near-field characterization for medical microwave imaging applications," *IEEE Trans. Antennas Propag.*, vol. 67, no. 7, pp. 4811–4824, Jul. 2019.
[23] MathWorks, "RCS," 2024. [Online]. Available: https://www.mathworks.com/help/antenna/ref/cavity.rcs.html
[24] Dassault Systemes, "CST studio suite," 2024. [Online]. Available: https://www.3ds.com/products/simulia/cst-studio-suite
[25] J. M. Felício, C. A. Fernandes, and J. R. Costa, "Complex permittivity and anisotropy measurement of 3D-printed PLA at microwaves and millimeter-waves," in *Proc. 22nd Int. Conf. Appl. Electromagnetics Commun.*, 2016, pp. 1–6.
[26] Ultimaker, "Professional 3D printing made accessible | Ultimaker," 2022. [Online]. Available: https://ultimaker.com/
[27] N. Joachimowicz, C. Conessa, T. Henriksson, and B. Duchêne, "Breast phantoms for microwave imaging," *IEEE Antennas Wireless Propag. Lett.*, vol. 13, pp. 1333–1336, 2014.
[28] K. Muinonen, "Introducing the Gaussian shape hypothesis for asteroids and comets," *Astron. Astrophys.*, vol. 332, pp. 1087–1098, 1998.



Raquel A. Martins was born in Queluz, Portugal, in 1995. She received the M.Sc. degree in electrical and computer engineering in 2019 from the Instituto Superior Técnico (IST), University of Lisbon, Lisbon, Portugal, where she is currently working toward the Ph.D. degree in electrical and computer engineering She is also a Researcher with the Instituto de Telecomunicações, Lisbon. Her research interests include microwave imaging, antenna design, and machine learning. She is currently a System Engineer with R&D Department in Nokia, Amadora, Portugal.



João M. Felício (Member, IEEE) received the M.Sc. and Ph.D. degrees in electrical and computer engineering from Instituto Superior Técnico (IST), University of Lisbon, Lisbon, Portugal, in 2014 and 2018, respectively. He is currently an Assistant Professor with Instituto Superior Técnico and a Researcher with the Instituto de Telecomunicações, Lisbon. He has coauthored more than 70+ technical papers in peer-reviewed international journals and conference proceedings. His interests include microwave imaging, antennas for biomedical and satellite applications, including mm-wave antennas, radiowave propagation, and machine learning applied to microwaves.



Jorge R. Costa (Senior Member, IEEE) was born in Lisbon, Portugal, in 1974. He received the Licenciado and Ph.D. degrees in electrical and computer engineering from the Instituto Superior Técnico (IST), Technical University of Lisbon, Lisbon, Portugal, in 1997 and 2002, respectively. He is currently a Senior Researcher with the Instituto de Telecomunicações, Lisbon. He is also a Full Professor with the Departamento de Ciências e Tecnologias da Informação, Instituto Universitário de Lisboa (ISCTE-IUL). His research interests include dielectric lenses, transmit-arrays, and biomedical antennas. He is the co-author of four patent applications and more than 250 contributions to peer-reviewed journals and international conference proceedings. More than fifty of these papers have appeared in IEEE Journals. He was an Associate Editor for IEEE TRANSACTIONS ON ANTENNAS AND PROPAGATION from 2010 to 2016 and he was a Guest Editor of the Special Issue on "Antennas and Propagation at mm- and Sub mm-Waves", from IEEE TRANSACTIONS ON ANTENNAS AND PROPAGATION, 2013. He is currently an Associate Editor for IEEE OPEN JOURNAL OF ANTENNAS AND PROPAGATION. He was the Co-Chair of the Technical Program Committee of the European Conference on Antennas and Propagation (EuCAP 2015) in Lisbon and General Vice-Chair of EuCAP 2017 in Paris, EuCAP 2021 online and EuCAP 2022 in Madrid.



Carlos A. Fernandes (Life Senior Member, IEEE) received the Licenciado, M.Sc., and Ph.D. degrees in electrical and computer engineering from Instituto Superior Técnico (IST), Technical University of Lisbon, Lisbon, Portugal, in 1980, 1985, and 1990, respectively. He joined IST in 1980, where he is currently a Full Professor with the Department of Electrical and Computer Engineering in the areas of microwaves, radio wave propagation and antennas. He is a Senior Researcher with Instituto de Telecomunicações. He has coauthored a book, book chapters, more than 350 technical papers in peer reviewed international journals and conference proceedings, and 8 patents in the areas of antennas and radiowave propagation modeling. His research interests include millimeter wave antennas for satellite applications and next generation mobile communications, and microwave imaging. He was a Guest Editor of the Special Issue on" Antennas and Propagation at mm- and Sub mm-Waves", from IEEE TRANSACTIONS ON ANTENNAS AND PROPAGATION, 2013.